RSC Advances

PAPER

View Article Online
View Journal | View Issue

Open Access Article. Published on 31 January 2020. Downloaded on 1/18/2026 12:14:17 AM.
This article is licensed under a Creative Commons Attribution-NonCommercial 3.0 Unported Licence.

Check for updates

Cite this: *RSC Adv.*, 2020, **10**, 5234

Facile and rapid synthesis of a novel spindle-like heterojunction $BiVO_4$ showing enhanced visible-light-driven photoactivity

Fang-yan Chen,* Xi Zhang, Yu-bin Tang,* Xin-gang Wang and Ke-ke Shu

A spindle-like monoclinic–tetragonal heterojunction $BiVO_4$ was successfully synthesized by a pressure-controllable microwave method. The as-prepared $BiVO_4$ samples were characterized by X-ray diffraction (XRD), scanning electron microscopy (SEM), transmission electron microscopy (TEM), X-ray photoelectron spectroscopy (XPS), UV-vis diffuse reflectance spectroscopy (DRS), photoluminescence (PL) spectroscopy, transient photocurrent responses and electrochemical impedance spectroscopy (EIS). The visible-light-driven photocatalytic activity of the $BiVO_4$ samples was evaluated for the degradation of Rhodamine B (RhB) and tetracycline (TC). The synthesis process needs microwave irradiation for only 10 min without the addition of any auxiliary reagent, pH adjustment, and calcination. The as-prepared spindle-like monoclinic–tetragonal heterojunction $BiVO_4$ exhibits excellent photocatalytic activity for the degradation of both RhB and TC. The photocatalytic degradation rates of RhB and TC over spindle-like $BiVO_4$ are 1.77 and 1.64 times higher, respectively, than that measured over monoclinic $BiVO_4$. The enhanced photocatalytic activity is mainly attributed to the fact that the existence of a heterojunction effectively promotes the separation of photo-generated carriers and extends the visible-light absorption of $BiVO_4$.

Received 29th September 2019
Accepted 27th December 2019

DOI: 10.1039/c9ra07891f

rsc.li/rsc-advances

Introduction

Over the past decades, photocatalysts have attracted considerable attention in the field of energy and environment.[1–5] Due to its high stability, low cost, non-toxicity and strong response to ultraviolet light, semiconductor oxide TiO_2 has been considered as an effective photocatalyst. However, the broad applications of TiO_2 are restricted because it can only utilize the ultraviolet (3–4%) fraction of the solar energy.[6,7] As a result, many researchers have been concentrating on investigating photocatalysts with visible-light-driven activity. $BiVO_4$ with a narrow band gap exhibits strong absorption of visible light and has been recognized as a promising visible-light-driven photocatalyst for the degradation of pollutants and water splitting.[8,9] As is known, $BiVO_4$ has three crystal types: tetragonal zircon type, tetragonal scheelite type, and monoclinic scheelite type. Of these, tetragonal zircon and monoclinic scheelite types are considered to possess photocatalytic properties. Tetragonal zircon type bismuth vanadate (t-$BiVO_4$) shows lower photocatalytic activity, while monoclinic bismuth vanadate (m-$BiVO_4$) exhibits higher activity. Nevertheless, poor adsorption performance and rapid recombination of photo-induced electrons and holes inhibit the efficient activity of m-$BiVO_4$. Therefore, various methods have been developed to improve the photocatalytic properties of $BiVO_4$. Morphological control has been proven to be an effective approach to enhance photocatalytic activity. Up to now, researchers have prepared many kinds of $BiVO_4$ with specific morphologies, such as tubular,[10] one-dimensional band,[11] rod-like,[12] two-dimensional sheet-shaped,[13] three-dimensional spherical,[14] multi-layer flower-like,[15] sandwich-like,[16] pumpkin-like,[17] and elliptical.[18] In addition, the construction of a monoclinic–tetragonal heterojunction is an ideal means to increase the photocatalytic activity.[19–21] At present, $BiVO_4$ materials with specific morphologies or monoclinic–tetragonal heterojunctions have been generally synthesized by the hydrothermal method that requires a very long time of more than 10 hours. Moreover, complicated processes, such as the use of solvents or auxiliary reagents, pH adjustment, calcination, and annealing treatment, are involved in hydrothermal preparations to obtain specific morphologies.

Microwave-assisted synthesis has been widely applied in synthesizing nanoscale inorganic materials due to homogeneous nucleation and rapid crystallization. The microwave-assisted preparation of the $BiVO_4$ photocatalyst has been reported by a few researchers.[22,23] Nevertheless, the microwave-assisted synthesis at normal pressure requires several hours. Recently, it has been reported that $BiVO_4$ can be successfully synthesized by a high-pressure microwave method.[24,25] The microwave-assisted synthesis of $BiVO_4$ under a high pressure can save reaction time and control morphology.

School of Environmental and Chemical Engineering, Jiangsu University of Science and Technology, Zhenjiang 212003, P. R. China. E-mail: chenfangyan@just.edu.cn

 This journal is © The Royal Society of Chemistry 2020

Open Access Article. Published on 31 January 2020. Downloaded on 1/18/2026 12:14:17 AM.
This article is licensed under a Creative Commons Attribution-NonCommercial 3.0 Unported Licence.

Herein, we report pressure-controllable microwave synthesis of a spindle-like monoclinic–tetragonal heterojunction $BiVO_4$. This synthesis method is facile and fast, only taking about 10 minutes of reaction time, without the addition of organic solvents and surfactants, adjustment of pH and calcination.

Experimental section

Preparation of $BiVO_4$

Here, 1.456 g of $Bi(NO_3)_3 \cdot 5H_2O$ was dissolved in 30 mL of deionized water and sonicated for 10 min to obtain solution A. Then, 0.36 g of $NaVO_3$ was dissolved in 20 mL of deionized water and sonicated for 10 min to obtain solution B. The solution B was added dropwise to the solution A under stirring. The obtained orange-yellow suspension was stirred at room temperature for 30 min and then transferred to a polytetrafluoroethylene digestion tank that was placed in a pressure-controllable microwave digestion apparatus for irradiation for 10 min. During the microwave irradiation, the microwave power, reactor pressure and reaction time were changed according to a pre-designed procedure (stage 1: microwave power 600 W, reactor pressure 5 kg cm^{-1},² reaction time 1.5 min; stage 2: microwave power 700 W, reactor pressure 10 kg cm^{-2}, reaction time 2 min; stage 3: microwave power 900 W, reactor pressure 15 kg cm^{-2}, reaction time 3.5 min; stage 4: microwave power 900 W, the reactor pressure 20 kg cm^{-2}, reaction time 3.5 min). The yellow products obtained after stage 2, stage 3 and stage 4 were washed with absolute ethanol and deionized water, dried at 80 °C, and marked as MB-2, MB-3, and MB-4, respectively.

For comparison, a single-phase m-$BiVO_4$ sample was prepared by the hydrothermal method and marked as HB. The preparation method of HB was as follows: 9.7 g of $Bi(NO_3)_3 \cdot 5H_2O$ was dissolved in 20 mL of 4 mol L^{-1} HNO_3 solution to form a transparent solution A. Then, 2.34 g of NH_4VO_3 was dissolved in 20 mL of 2 mol L^{-1} NaOH solution to obtain solution B. The solution B was added dropwise to the solution A under stirring and was further stirred for 2 hours at room temperature. The pH of the mixture was adjusted to 7 with NaOH to give an orange-yellow solution. The orange-yellow solution was added to a 100 mL Teflon reactor and heated at 180 °C for 24 h. The product was naturally cooled to room temperature, washed with water and ethanol several times, and dried at 80 °C to obtain a $BiVO_4$ sample HB.

Characterization of $BiVO_4$

The XRD patterns of the samples were recorded on a D8 Advance X-ray diffractometer (Bruker, Germany) using Cu-Kα radiation (λ = 1.5406 Å). The SEM and TEM images of the samples were observed on an S-4800 field emission scanning electron microscope (Hitachi, Japan) and a JEM-2100 transmission electron microscope (Japan Electronics, Japan), respectively. UV-vis diffuse reflectance spectra were obtained on a UV-2550 UV-vis spectrophotometer (Shimadzu, Japan) using $BaSO_4$ as a reflectance standard. The XPS spectra were collected on an ESCALAB-250i X-ray photoelectron spectroscope (Thermo Fisher Scientific, USA). PL spectra were recorded on an F4500 fluorescence spectrometer. Transient photocurrent responses and EIS of the sample were measured on a CHI 660D electrochemical workstation (Chenhua Instrument, China) with an FTO electrode deposited with a catalyst as the working electrode using Na_2SO_4 aqueous solution of 0.1 mol L^{-1} as an electrolyte under visible-light illumination.

Photocatalytic activity test

The photocatalytic activity was evaluated for the degradation of Rhodamine B (RhB) and tetracycline (TC) under visible-light irradiation. Typically, 100 mg of $BiVO_4$ was added to 100 mL of RhB or TC solution with a concentration of 5 mg L^{-1} and stirred for 30 min in the dark for adsorption–desorption equilibrium. Then, the solution was irradiated by a 300 W xenon lamp with a 420 nm cut-off filter. Three mL of the solution was sampled at 15 min intervals. The concentrations of RhB and TC in the solution were analysed on a UV-Vis spectrophotometer at the wavelengths of 554 and 357 nm, respectively.

Results and discussion

XRD analysis

Fig. 1 shows the XRD patterns of the samples. The diffraction peaks of HB are completely consistent with those expected for m-$BiVO_4$ (standard card number JCPDS No. 14-0688), indicating that $BiVO_4$ prepared by the hydrothermal method is a pure phase of m-$BiVO_4$. In the XRD patterns of MB-2, MB-3 and MB-4, not only the diffraction peaks at 18.5°, 28.8°, and 30.5°, but also the peaks at 24.5°, 32.6°, and 39.5° appeared. The peaks at 18.5°, 28.8°, and 30.5° belong to the (110), (121), and (040) crystal planes of m-$BiVO_4$, respectively. In contrast, the diffraction peaks at 24.5°, 32.6°, and 39.5° correspond to the (200), (112), and (301) crystal planes of t-$BiVO_4$ (standard card number JCPDS No. 14-0133). It is suggested that MB-2, MB-3 and MB-4 prepared at different reaction stages are the composites of m-$BiVO_4$ and t-$BiVO_4$. Moreover, compared with the diffraction

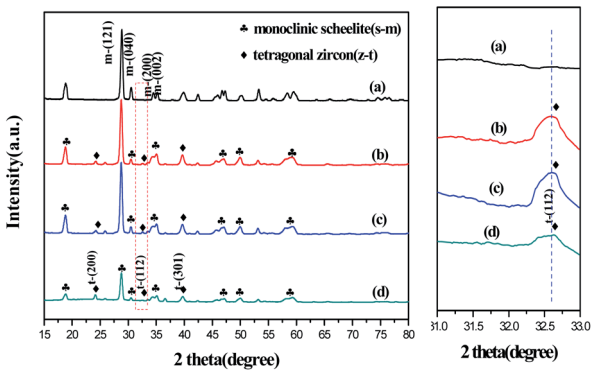

Fig. 1 XRD patterns of HB (a), MB-2 (b), MB-3 (c) and MB-4 (d).

Open Access Article. Published on 31 January 2020. Downloaded on 1/18/2026 12:14:17 AM.
This article is licensed under a Creative Commons Attribution-NonCommercial 3.0 Unported Licence.

peak intensities of HB, MB-2, and MB-3, the diffraction peak intensity of MB-4 at 18.5°, 28.8°, and 30.5° weakened with the broadening of the peaks. According to formula (1),[26] the proportions of tetragonal $BiVO_4$ in the MB-2, MB-3, and MB-4 composites were estimated to be 6.3%, 3.5%, and 23%, respectively.

$$\eta_{\text{tetra}} = I_{\text{tetra}(200)}/(I_{\text{tetra}(200)} + I_{\text{mono}(121)}) \quad (1)$$

Here, η_{tetra} represents the proportion of the tetragonal phase. $I_{\text{tetra}(200)}$ and $I_{\text{mono}(121)}$ are the relative intensities of the diffraction peaks of the tetragonal phase (200) and monoclinic phase (121), respectively.

Thus, the XRD results indicated that $BiVO_4$ was obtained only within 3.5 min under microwave irradiation with the microwave reaction pressure increasing from 5 kg cm^{-2} to 10 kg cm^{-2}. This is due to the acceleration of the precipitation and crystallization of $BiVO_4$ under high-pressure microwave conditions. Furthermore, microwave pressure plays a significant role in the phase transition of $BiVO_4$. By increasing the reaction pressure and time, the transformation from m-$BiVO_4$ to t-$BiVO_4$ was achieved. The probable reason is that m-$BiVO_4$ was thermodynamically more stable under the condition of 5 kg cm^{-2} to 10 kg cm^{-2} pressure; thus, MB-2 obtained in stage 2 mainly consists of m-$BiVO_4$. In stage 3 and 4, increased pressure resulted in partial dissolution–recrystallization of m-$BiVO_4$ formed in stage 2 to form a composite of m-$BiVO_4$ and t-$BiVO_4$.

SEM and TEM

The morphology of the samples was investigated using SEM and TEM (Fig. 2). The SEM image in Fig. 2(a) indicates that m-$BiVO_4$ prepared by the hydrothermal method is in the form of flakes with some agglomeration and size of about 1 μm.

Fig. 2(b–d) reveal that the $BiVO_4$ samples prepared by the microwave method appear as spindle-like particles with a rough surface and length of about 10 μm, which are constructed by the assembly of many sheet-shaped particles of uniform diameter. It was indicated that the spindle-like morphology was formed at stage 2 with a microwave power of 700 W and a reactor pressure of 10 kg cm^{-2}. Nevertheless, the $BiVO_4$ sample MB-4 obtained in stage 4 had more regular and perfect spindle-like morphology. The TEM image of MB-4 (Fig. 2(e)) confirms the solid construction of spindle-like $BiVO_4$. Fig. 2(f) and (g) show the high-resolution TEM images of MB-4. In Fig. 2(f), the crystal planes with the lattice fringe spacings of 0.312 nm and 0.182 nm belong to the (121) plane of m-$BiVO_4$ and the (400) plane of t-$BiVO_4$, respectively. The (121) plane of m-$BiVO_4$ is evidently in close contact with the (400) plane of t-$BiVO_4$. Fig. 2(e) shows that the (110) plane of m-$BiVO_4$ is in close contact with the (112) plane of t-$BiVO_4$. Therefore, it is concluded that the heterojunction is formed between m-$BiVO_4$ and t-$BiVO_4$.

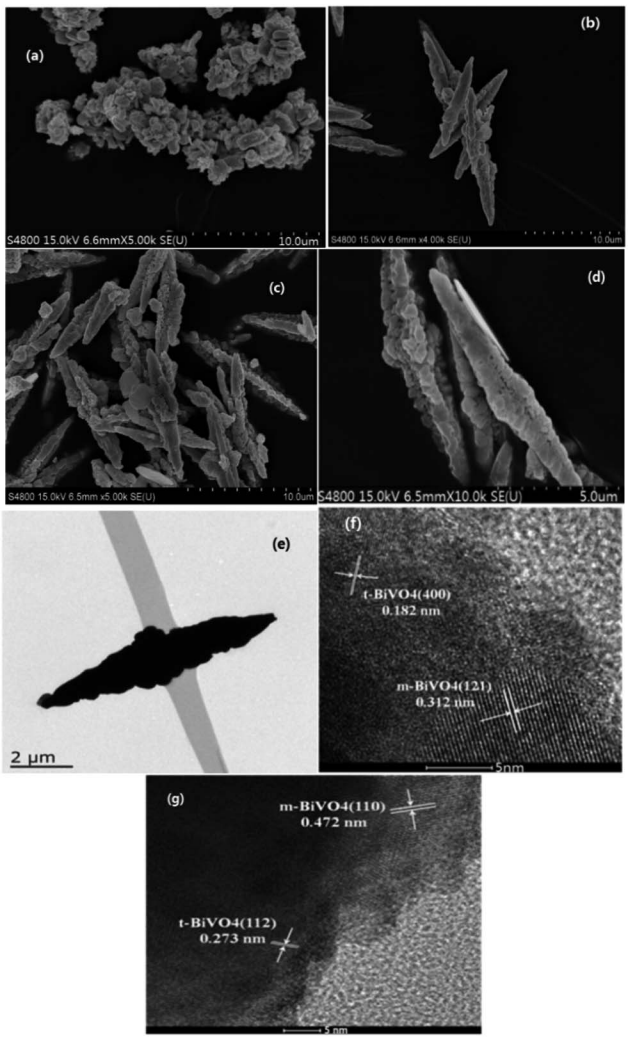

Fig. 2 SEM images of HB (a) and MB-2 (b), MB-2 (c), MB-4 (d). TEM image of MB-4 (e) and HRTEM images of MB-4 (f and g).

X-ray photoelectron spectroscopy (XPS) analysis

X-ray photoelectron spectroscopy (XPS) was conducted to investigate the chemical state and surface composition of the sample. The XPS spectra of MB-4 based on C1s are presented in Fig. 3.

It is observed from the XPS survey spectrum (Fig. 3(a)) that MB-4 consists of Bi, V and O. In the high-resolution spectrum of Bi (Fig. 3(b)), the peaks at 159.2 eV and 164.5 eV are assigned to Bi 4f7/2 and Bi 4f5/2, respectively, which indicates that the bismuth element in the spindle-like $BiVO_4$ exists as Bi^{3+}.[27] The peaks at 523.9 eV and 516.6 eV in Fig. 3(c) are characteristic spin–orbit splitting signals of V 2p1/2 and V 2p3/2, respectively, suggesting that all the vanadium species in the $BiVO_4$ sample are present in the pentavalent state.[28] The O1s spectra (Fig. 3(d)) can be differentiated into two peaks with the binding energies of 529.8 eV and 531.2 eV, which are attributed to the lattice oxygen of $BiVO_4$ and adsorbed oxygen such as surface-adsorbed $^{\bullet}OH$ and H_2O, respectively. It is universally known that higher adsorbed oxygen means more oxygen vacancies, which will result in the enhancement in the photocatalytic activity.[29]

Open Access Article. Published on 31 January 2020. Downloaded on 1/18/2026 12:14:17 AM.
This article is licensed under a Creative Commons Attribution-NonCommercial 3.0 Unported Licence.

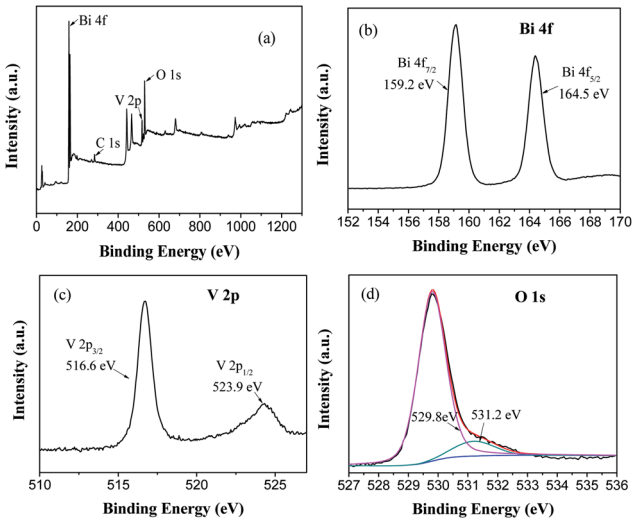

Fig. 3 XPS survey spectra of MB-4 (a) and high-resolution XPS spectra of Bi 4f (b), V 2p (c), O 1s (d).

BET surface area

The N_2 adsorption–desorption isotherm and the Barrett–Joyner–Halenda plot for the pore size distribution of MB-4 are shown in Fig. 4.

As seen in Fig. 4, the pores have a diameter of 10–80 nm; the average pore diameter is 32.204 nm. Based on the Brunauer–Emmett–Teller (BET) model, the surface area of MB-4 is estimated to be 1.596 $m^2\ g^{-1}$. The small specific surface area is perhaps due to the fact that MB-4 is a large micron-sized particle, which is tightly assembled by a large number of nanosized sheet-shaped $BiVO_4$.

UV-vis diffuse reflectance spectroscopy (DRS)

The optical absorption property of a semiconductor is considered as a crucial factor for its photocatalytic performance. UV-vis diffuse reflectance spectroscopy was used to detect the optical response characteristics of the sample. Fig. 5(a) shows the UV-vis diffuse reflectance spectra of HB and MB-4. As seen from Fig. 5(a), both the samples display strong absorption in the visible-light region, which is due to the migration of an electron from the Bi 6s and O 2p orbitals to the V 3d orbitals.[30]

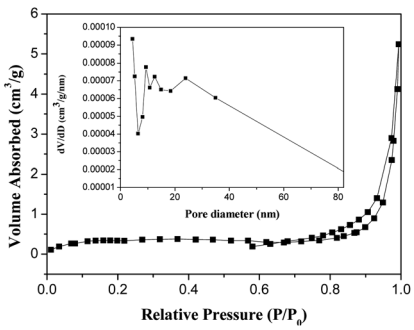

Fig. 4 Nitrogen adsorption–desorption isotherm and pore size distribution plot of MB-4.

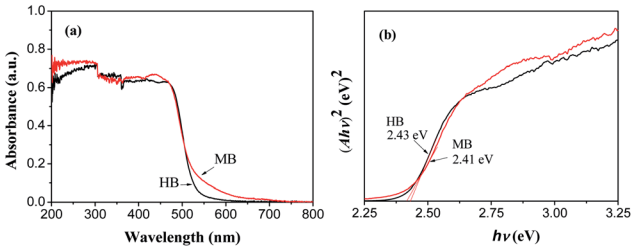

Fig. 5 UV-vis diffuse reflectance spectra of HB and MB-4.

The absorption edge of HB is around 520 nm, while the absorption edge of MB-4 shifts to 550 nm. It is concluded that the spindle-like $BiVO_4$ heterojunction synthesized by the microwave method has superior visible-light response characteristics to those of m-$BiVO_4$.

The band gap values of a semiconductor can be estimated by the Tauc formula $\alpha h\nu = A(h\nu - E_g)^{n/2}$, where α is the absorption coefficient, h is the Planck constant, and ν is the optical frequency; A is a constant and E_g is the band gap energy of the semiconductor.[31] For $BiVO_4$, a direct bandgap semiconductor, the value of n is 1.[32] According to the Tauc formula, a plot of $(\alpha h\nu)^2$ *versus* $(h\nu)$ is obtained and shown in Fig. 5(b). The E_g values of m-$BiVO_4$ and spindle-like $BiVO_4$, obtained from the intercept of the tangent of the curve of $(\alpha h\nu)^2$ *versus* $(h\nu)$ on the X-axis, are 2.43 eV and 2.41 eV, respectively. The band gap of spindle-like $BiVO_4$ is less than that of m-$BiVO_4$.

The conduction and valence band potentials of a semiconductor can be determined by following eqn (2) and (3):[21,24]

$$E_{VB} = X - E_e + 0.5E_g \quad (2)$$

$$E_{CB} = E_{VB} - E_g \quad (3)$$

Here, E_{VB} and E_{CB} are the conduction and valence band potentials, respectively. E_g is the band-gap energy of the semiconductor, E_e is the energy of the free electrons on the hydrogen scale (about 4.5 eV), and X is the electronegativity of the semiconductor. The X value for $BiVO_4$ is 6.04 eV. According to eqn (2) and (3), the conduction and valence band potentials of m-$BiVO_4$ are obtained as 0.32 eV and 2.75 eV, respectively.

Photocatalytic property

The photocatalytic property of the as-prepared $BiVO_4$ was evaluated for the degradation of RhB and tetracycline (TC) under the irradiation of visible light. Fig. 6(a) shows that the degradation rate of RhB over MB-4 is high and up to 90.8% after 180 min of irradiation. However, the degradation rate of RhB over HB is 70.9%. Fig. 6(b) reveals that the degradation rate of TC over MB-4 is 78.9% within 180 min, while the degradation rate of TC over HB is 61.9%. For the degradation of both RhB and TC, the photocatalytic activity of the spindle-like heterojunction $BiVO_4$ (MB-4) is significantly higher than that of single-phase m-$BiVO_4$ (HB). Hence, the spindle-like heterojunction $BiVO_4$ exhibits excellent photocatalytic activity for the degradation of RhB and TC.

Open Access Article. Published on 31 January 2020. Downloaded on 1/18/2026 12:14:17 AM.
This article is licensed under a Creative Commons Attribution-NonCommercial 3.0 Unported Licence.

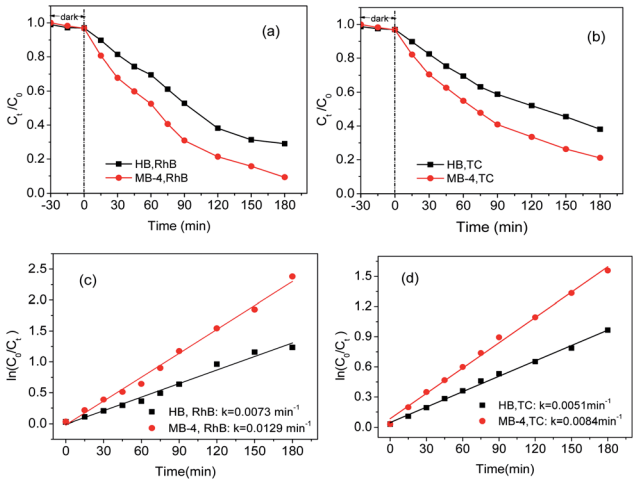

Fig. 6 (a) Photodegradation of RhB, (b) photodegradation of TC under visible light, (c) kinetics of degradation of RhB and (d) kinetics of degradation of TC.

It is well-known that the photocatalytic degradation of organic pollutants follows apparent first-order kinetics expressed as eqn (4).[33]

$$\ln(C_t/C_0) = -kt \tag{4}$$

Here, C_0 and C_t represent the concentrations of RhB at the initial time and t time, respectively; k is the apparent reaction constant. As can be seen from Fig. 6(c), the k value of RhB over MB-4 is 0.0129 min^{-1}, which is 1.77 times higher than that of RhB over HB. Fig. 6(d) indicates that the k value of TC over MB-4 is 0.0084 min^{-1}, which is 1.64 times higher than that of TC over HB. Compared with the photocatalytic activity of HB, the enhanced photocatalytic activity of MB-4 is probably due to the surface-phase junctions formed between m-$BiVO_4$ and t-$BiVO_4$ and the red shift in the absorption edge of MB-4.

To evaluate the stability of spindle-like $BiVO_4$, cyclic degradation experiments were carried out and the results are shown in Fig. 7. It can be found that the photocatalytic activity of the spindle-like $BiVO_4$ does not decrease even after four cycling runs, confirming its excellent stability and reusability under visible light.

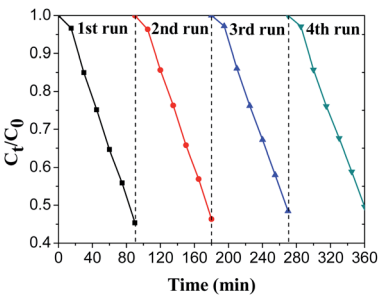

Fig. 7 Recycling runs of the spindle-like $BiVO_4$ for photocatalytic degradation of RhB.

Photoluminescence (PL) spectra

To probe a possible reason for the higher photocatalytic activity of MB-4, PL spectra were obtained to investigate the recombination probability of electron–hole pairs. Fig. 8 gives the PL spectra of HB and MB-4. As shown in Fig. 8, the PL spectra of MB-4 and HB are substantially similar, and a strong emission peak is observed at about 708 nm. However, compared with the observation for HB, the PL emission intensity of MB-4 weakened, suggesting that the recombination of electrons and holes in the spindle-like $BiVO_4$ was effectively inhibited.

Transient photocurrent responses and EIS

In order to further investigate the separation and transfer of photo-induced charges, transient photocurrent responses and EIS studies were conducted. Fig. 9(a) gives the transient photocurrent response of MB-4 and HB. MB-4 exhibits remarkably higher photocurrent than that shown by HB, indicating more efficient separation of electron–hole pairs in spindle-like $BiVO_4$.[34] Fig. 9(b) shows the EIS results of MB-4 and HB. It is found that MB-4 has an obviously smaller radius than HB, further confirming that the charge transfer in spindle-like $BiVO_4$ is significantly faster than that in pure m-$BiVO_4$. It is because the interface of tetragonal–monoclinic heterojunction can promote the separation of photo-generated electron–hole pairs.[35,36] Thus, the relatively high photocatalytic activity of MB-4 is mainly attributed to a smaller recombination rate of photo-induced carriers and its better optical absorption capacity.

Detection of active species

To further explore the probable mechanism of charge carriers transferring in MB-4, the active species produced during the photocatalytic degradation of RhB over MB-4 were identified by a free radical trapping test. EDTA-2Na, isopropanol, and p-benzoquinone were selected as scavengers to be added into the RhB solution to remove the holes (h^+), hydroxyl radicals ($^{\bullet}OH$) and superoxide radicals ($^{\bullet}O_2^-$), respectively. The photocatalytic activity of RhB in the presence of scavengers is given in Fig. 10. As can be seen, the addition of EDTA-2Na results in a significant decrease in the photocatalytic degradation of RhB. In the presence of p-benzoquinone, the photocatalytic activity of the MB-4 sample is slightly inhibited. However, the degradation of RhB has no obvious decrease when isopropanol is used as

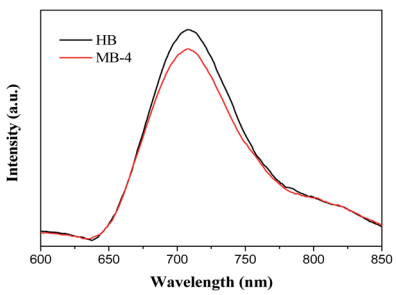

Fig. 8 Photoluminescence spectra of HB and MB-4.

Open Access Article. Published on 31 January 2020. Downloaded on 1/18/2026 12:14:17 AM.
This article is licensed under a Creative Commons Attribution-NonCommercial 3.0 Unported Licence.

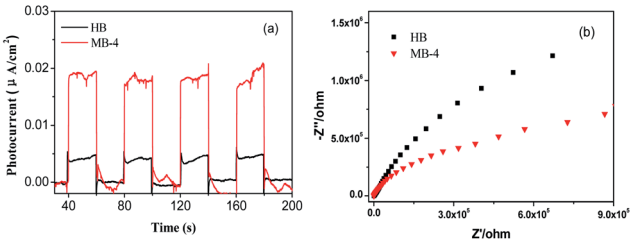

Fig. 9 (a) Transient photocurrent response and (b) EIS of MB-4 and HB.

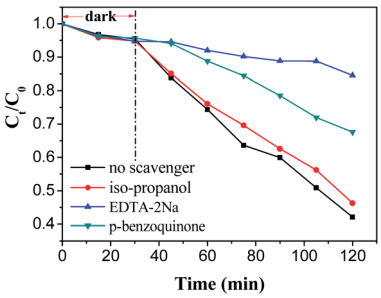

Fig. 10 Photodegradation of RhB over MB-4 in the presence of different scavengers.

a scavenger. Therefore, it is indicated that the holes mainly account for the degradation of RhB.

Probable mechanism

According to our experimental results, E_{CB} and E_{VB} of m-$BiVO_4$ are 0.32 eV and 2.75 eV, respectively. In contrast, E_{CB} and E_{VB} of t-$BiVO_4$ have been reported in a reference to be 0.24 eV and 2.84 eV, respectively.[21] Based on the results about the conduction band and valence band potentials, transient photocurrent responses and active species, the possible charge migration during the photocatalytic degradation of RhB is speculated and shown in Fig. 11. Both m-$BiVO_4$ and t-$BiVO_4$ are excited by visible light to generate electrons and holes. The photo-generated electrons on the conduction band of t-$BiVO_4$ migrate to the conduction band of m-$BiVO_4$ because the conduction band of m-$BiVO_4$ is below the conduction band of t-$BiVO_4$. At the same time, the photo-induced holes on the valence band of t-$BiVO_4$ can be easily transferred to the valence band of m-$BiVO_4$. Consequently, the photo-generated electron–hole pairs are effectively separated. The holes with significantly positive potential on the surface can directly oxidize RhB.

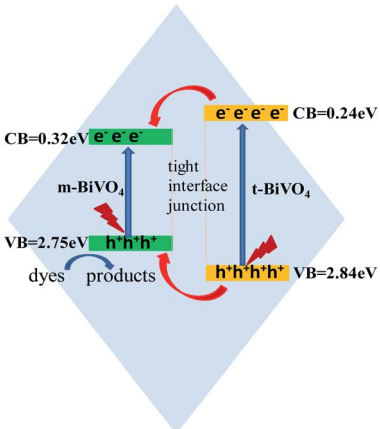

Fig. 11 Illustration of probable charge transfer on the interface junction of m-$BiVO_4$ and t-$BiVO_4$.

Conclusions

A spindle-like $BiVO_4$ was successfully synthesized using a pressure-controllable microwave method. The synthesis process was facile and rapid without the addition of any auxiliary reagent, adjustment of pH and annealing. It is found that the as-prepared spindle-like $BiVO_4$ is a heterojunction composed of monoclinic scheelite $BiVO_4$ and tetragonal zircon $BiVO_4$. The existence of a heterojunction effectively promotes the separation of photo-generated carriers, which enhances the activity of spindle-like $BiVO_4$ compared to that of monoclinic phase $BiVO_4$. The photocatalytic degradation rates of RhB and TC over spindle-like $BiVO_4$ are 1.77 and 1.64 times higher, respectively, than that over monoclinic $BiVO_4$. Under visible-light illumination, the photo-induced electrons from the conduction band of t-$BiVO_4$ migrate to the conduction band of m-$BiVO_4$, while the photo-generated holes from the valence band of t-$BiVO_4$ are transferred to the valence band of m-$BiVO_4$. In this way, the photo-generated electron–hole pairs are effectively separated. The holes on the surface directly degrade RhB and TC.

Conflicts of interest

There are no conflicts of interest to declare.

Acknowledgements

This work is supported by the Postgraduate Research & Practice Innovation Program of Jiangsu Province (China) (SJKY19_2658, SJKY19_2629).

References

1 S. Adhikari and D. Sarkar, *Mater. Res. Bull.*, 2015, **72**, 220–228.
2 M. Y. Li, Y. B. Tang, W. L. Shi, F. Y. Chen, Y. Shi and H. C. Gu, *Inorg. Chem. Front.*, 2018, **5**, 3148–3154.
3 J. Xu, B. F. Luo, W. Gu, Y. P. Jian, F. L. Wu, Y. B. Tang and H. Shen, *New J. Chem.*, 2018, **42**, 5052–5058.
4 F. P. Cai, Y. B. Tang, F. Y. Chen, Y. Yan and W. D. Shi, *RSC Adv.*, 2015, **5**, 21290–21296.
5 Y. X. Wang, H. Wang, F. Y. Chen, F. Cao, X. H. Zhao, S. G. Meng and Y. J. Cui, *Appl. Catal., B*, 2017, **206**, 417–425.
6 G. Jiang, X. Wang, Z. Wei and X. Li, *J. Mater. Chem. A*, 2013, **1**, 2406–2410.
7 G. Jiang, Z. Wei, H. Chen and X. X. Du, *RSC Adv.*, 2015, **5**, 30433–30437.

Open Access Article. Published on 31 January 2020. Downloaded on 1/18/2026 12:14:17 AM.
This article is licensed under a Creative Commons Attribution-NonCommercial 3.0 Unported Licence.

8 G. Xi and J. Ye, *Chem. Commun.*, 2010, **46**, 1893–1895.
9 Y. Wang, J. Huang, G. Tan, J. Huang and L. Zhang, *Nano*, 2015, **10**, 78–86.
10 C. Lv, J. Sun, G. Chen, Y. Zhou and D. Li, *Appl. Catal., B*, 2017, **208**, 14–21.
11 F. Wang, M. Shao, C. Liang, J. Hua and X. Wei, *Mater. Res. Bull.*, 2009, **44**, 1687–1691.
12 B. Liu, X. Yan, H. Yan, Y. Yao, Y. Cai, J. Wei, S. Chen, X. Xu and L. Li, *Materials*, 2017, **10**, 976–986.
13 D. Wang, H. Jiang, X. Zong, Q. Xu, Y. Ma, G. Li and C. Li, *Chemistry*, 2011, **17**, 1275–1282.
14 H. Q. Jiang, H. Endo, H. Natori, M. Nagai and K. Kobayashi, *J. Eur. Ceram. Soc.*, 2008, **28**, 2955–2962.
15 H. B. Li, J. Zhang, G. Y. Huang, S. H. Fu, C. Ma, B. Y. Wang, Q. R. Huang and H. W. Liao, *Trans. Nonferrous Met. Soc. China*, 2017, **27**, 868–875.
16 S. Liu, H. Tang, H. Zhou, G. Dai and W. Wang, *Appl. Surf. Sci.*, 2016, **391**, 542–547.
17 L. Ye, L. Li, L. Guo, H. Peng and K. Chen, *Mater. Lett.*, 2017, **221**, 171–174.
18 Y. Lu, H. Shang, F. Shi, C. Chao, X. Zhang and B. Zhang, *J. Phys. Chem. Solids*, 2015, **85**, 44–50.
19 D. T. Nguyen and S. S. Hong, *Top. Catal.*, 2017, **60**, 782–788.
20 N. D. Phu, L. H. Hoang, P. K. Vu, M. H. Kong, X. B. Chen, H. C. Wen and W. C. Chou, *J. Mater. Sci.: Mater. Electron.*, 2016, **27**, 6452–6456.
21 W. Li, X. Wang, Z. Wang, Y. Meng, X. Sun, T. Yan, J. You and D. Kong, *Mater. Res. Bull.*, 2016, **83**, 259–267.
22 W. Shi, Y. Yan and X. Yan, *Chem. Eng. J.*, 2013, **215–216**, 740–746.
23 S. Moscow and K. Jothivenkatachalam, *J. Mater. Sci.: Mater. Electron.*, 2015, **27**, 1433–1443.
24 T. S. Dabodiya, P. Selvarasu and A. V. Murugan, *Inorg. Chem.*, 2019, **58**, 5096–5110.
25 Y. Wang, F. Liu, Y. Hua, C. Wang, X. Zhao, X. Liu and H. Li, *J. Colloid Interface Sci.*, 2016, **483**, 307–313.
26 A. K. Bhattacharya, K. K. Mallick and A. Hartridge, *Mater. Lett.*, 1997, **30**, 7–13.
27 B. Zhou, J. Qu, Z. Xu and H. Liu, *J. Environ. Sci.*, 2011, **23**, 151–159.
28 J. Su, X. X. Zou, G. D. Li, X. Wei, C. Yan, Y. N. Wang, J. Zhao, L. Zhou and J. Chen, *J. Phys. Chem. C*, 2011, **115**, 8064–8071.
29 M. Wang, Y. S. Che, C. Niu, M. Dang and D. Dong, *J. Rare Earths*, 2013, **31**, 878–884.
30 K. Sayama, A. Nomura, Z. Zou, R. Abe, Y. Abe and H. Arakawa, *Chem. Commun.*, 2004, 2908–2909.
31 Z. Zhu, J. Du, J. Li, Y. Zhang and D. Liu, *Ceram. Int.*, 2012, **38**, 4827–4834.
32 Z. Lin, W. Wang, S. Liu, L. Zhang, H. Xu and W. Zhu, *J. Mol. Catal. A: Chem.*, 2006, **252**, 120–124.
33 W. Y. Jung and S. S. Hong, *J. Ind. Eng. Chem.*, 2013, **19**, 157–160.
34 Z. H. Wei, Y. F. Wang, Y. Y. Li, L. Zhang, H. C. Yao and Z. J. Li, *J. CO2 Util.*, 2018, **28**, 15–25.
35 N. D. Phu, L. H. Hoang, P. K. Vu, M. H. Kong, X. B. Chen, H. C. Wen and W. C. Chou, *J. Mater. Sci.: Mater. Electron.*, 2016, **27**, 6452–6456.
36 X. Gao, H. B. Wu, L. Zheng, Y. Zhong, Y. Hu and X. W. Lou, *Angew. Chem., Int. Ed.*, 2013, **53**, 5917–5921.

 This journal is © The Royal Society of Chemistry 2020